PHYSICAL REVIEW B **104**, 075420 (2021)

Andreev reflection in Fermi-arc surface states of Weyl semimetals

Yue Zheng,[1] Wei Chen,[1,2,*] and D. Y. Xing[1,2]
[1]*National Laboratory of Solid State Microstructures and School of Physics, Nanjing University, Nanjing 210093, China*
[2]*Collaborative Innovation Center of Advanced Microstructures, Nanjing University, Nanjing 210093, China*

(Received 28 October 2020; accepted 30 July 2021; published 12 August 2021)

Fermi-arc surface states are the hallmark of Weyl semimetals, whose identification is usually challenged by their coexistence with gapless bulk states. Surface transport measurements by fabricating setups on the sample boundary provide a natural solution to this problem. Here, we study the Andreev reflection (AR) in a planar normal metal-superconductor junction on the Weyl semimetal surface with a pair of Fermi arcs. For a conserved transverse momentum, the occurrence of normal reflection depends on the relative orientation between the Fermi arcs and the normal of the junction, which is a direct result of the disconnected Fermi arcs. Consequently, a crossover from the suppressed to perfect AR occurs with varying the orientation of the planar junction, giving rise to a change from double-peak to plateau structure in conductance spectra. Moreover, such a crossover can be facilitated by imposing a magnetic field, making electrons slide along the Fermi arcs so as to switch between two regimes of the AR. Our results provide a decisive signature for the detection of Fermi arcs and open the possibilities of exploring novel phenomenology through their interplay with superconductivity.

DOI: 10.1103/PhysRevB.104.075420

I. INTRODUCTION

In 1929, Weyl proposed a new type of massless fermion with definite chirality [1]. After that, great efforts have been made in pursuing such elemental particles in high-energy particle physics [2], yet up until now, no candidate Weyl fermion has been reported [3,4]. In recent years instead, Weyl fermions are surprisingly found in an alternative form of quasiparticle excitations in a class of solid-state materials with conic band crossing, called Weyl semimetals (WSMs) [5]. The discovery of the WSM opens up a new avenue for the study of relativistic Weyl fermion in condensed matter physics [6–22]. It provides an interesting platform for the experimental testing of predictions made by quantum field theory [23–25] in terms of anomalous transport and optical properties in the condensed matter context [26–44].

In addition to its high-energy counterpart, WSM also exhibits unique properties that exist only in the condensed matter context, especially the emergence of Fermi-arc (FA) surface states on the sample boundaries [5]. In WSMs, Weyl points always appear in pairs with opposite topological charge (chirality) [25], the FA spanning between each pair in the surface Brillouin zone [5]. Such disconnected FAs cannot be realized in any noninteracting two-dimensional (2D) bulk states so that its emergence can serve as the hallmark of WSMs [9–22]. It was recently shown that the configurations of the FA are sensitive to the details of the sample boundary [45–47], which opens the possibility for engineering FA and exploring its applications through surface modification. With this prospect, it is of great importance to extract and analyze clear signatures of the FA from measurement information in the presence of gapless bulk states. Surface transport measurements provide a natural solution to this goal because the setups contact directly to the sample boundaries [48,49].

In this work, we propose that Andreev reflection (AR) in a planar normal metal (N)-superconductor (S) junction on the WSM surface can provide a unique signature of the FA. The junction consists of two parallel N and S strip electrodes mediated by the topological surface states in between; see Fig. 1(a). For the unclosed FA, there generally exist two regions of different AR scenarios, referred to as I and II in Fig. 1(c). In region I, no normal reflection channel is available [Fig. 1(a)] so that there is a perfect AR with probability equal to unity within the energy gap [cf. Fig. 2(c)], in spite of the interface barrier. On the contrary, AR is strongly suppressed in region II by normal reflection at the boundary of the S [Fig. 1(b)], which results in a pair of resonant peaks of the AR probability at the gap edges [cf. Fig. 2(a)]. The proportion of electrons in two regions relies on the relative orientation between the WSM and the normal of the planar junction. This leads to a crossover between the double-peak and plateau structures in the conductance spectra by changing the orientation of the planar junction in different samples [Fig. 2(d)]. Two limiting cases occur as the electrons reside entirely in region I or II [Figs. 2(a) and 2(c)]. Remarkably, such a crossover can be greatly facilitated by imposing a magnetic field to a properly orientated planar junction such that the two AR regions coexist. The magnetic field drives electrons sliding along the FA and simultaneously opens up a transport channel in the bulk, i.e., the chiral Landau band, connected with the surface FA [50]. As a result, part of the electrons can switch between the two AR regions while the remaining ones penetrate the bulk with negligible contribution to the surface transport signature. In this way, the same crossover behavior of the conductance can be achieved along with a reduction of its magnitude. The

---

[*] Corresponding author: pchenweis@gmail.com

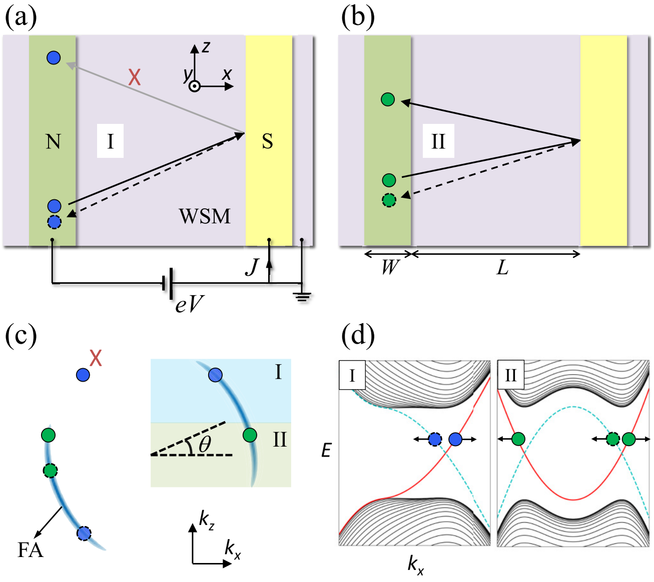

FIG. 1. (a),(b) Schematic of the planar normal metal (N)-superconductor (S) junction on top of the WSM and the scattering of particles at the interface. The trajectories of electron (solid circle) and hole (dashed circle) are sketched as the solid and dashed lines, respectively. (c) Two regions I and II for AR are defined by the transverse momentum k_z. (d) Band structures for a fixed k_z in region I and II. The red solid and blue dashed lines are the electron and hole surface states.

AR spectra have the advantage that two scenarios can be clearly revealed by different shapes of the conductance rather than its magnitude, which provides a distinctive and robust signature of the FAs.

The rest of this paper is organized as follows. In Sec. II, we introduce the model and calculation details. In Sec. III, we show that a crossover of the conductance from the suppressed to perfect AR can be achieved by varying the orientation of the planar junction. We show that such an effect can be facilitated by the magnetic field in Sec. IV. Finally, some remarks are given in Sec. V.

II. MODEL AND CALCULATION DETAILS

We consider a WSM with four Weyl points, which can be captured by the effective two-band model as [49]

$$H_W^0(\boldsymbol{k}) = M_1\left(k_1^2 - k_x^2\right)\sigma_x + v_y k_y \sigma_y + M_2\left(k_0^2 - k_y^2 - k_z^2\right)\sigma_z, \tag{1}$$

where v_y is the velocity in the y direction, $k_{0,1}$ and $M_{1,2}$ are parameters, $\sigma_{x,y,z}$ are the Pauli matrices in the pseudospin space. The two bands are degenerate at four Weyl points $\boldsymbol{k}_W = (\pm k_1, 0, \pm k_0)$. The main results of this work are associated with the relative orientation between the FAs and the planar junction. We define θ as the azimuthal angle between the symmetry axis of the FA and the normal of the junction (set to the x axis); see Fig. 1(c). Experimentally, this can be alternatively realized by fabricating various planar junctions along different directions. The FAs with azimuthal angle θ correspond to the rotated Hamiltonian $H_W(\boldsymbol{k}) = H_W^0(U_y^{-1}\boldsymbol{k})$ with $U_y(\theta) = \begin{pmatrix} \cos\theta & 0 & -\sin\theta \\ 0 & 1 & 0 \\ \sin\theta & 0 & \cos\theta \end{pmatrix}$ as the rotation operator around the y axis [51].

The configurations of the FAs are revealed by the spectra function $\mathcal{A}(E) = -(1/\pi)\mathrm{Im}G^R(E)$, where $G^R(E)$ is the retarded Green's function, under the open boundary condition in the y direction. To yield curved FAs similar to those in real materials [47,52–54], an on-site potential is imposed to the top layer of the WSM lattice, which modifies the dispersion of the surface states [49] through surface band bending effect [55–57] . The FAs for different azimuthal angle θ are shown in Figs. 2(a)–2(c).

To investigate the AR, we write the Hamiltonian for the whole system in Nambu space. The electron and hole components are decoupled in the WSM so that the Bogoliubov–de Gennes Hamiltonian takes a diagonal form of $\mathcal{H}_W(\boldsymbol{k}) = [H_W^0(\boldsymbol{k}), 0; 0, -H_W^{0*}(-\boldsymbol{k})]$. For a given k_z, the Hamiltonian

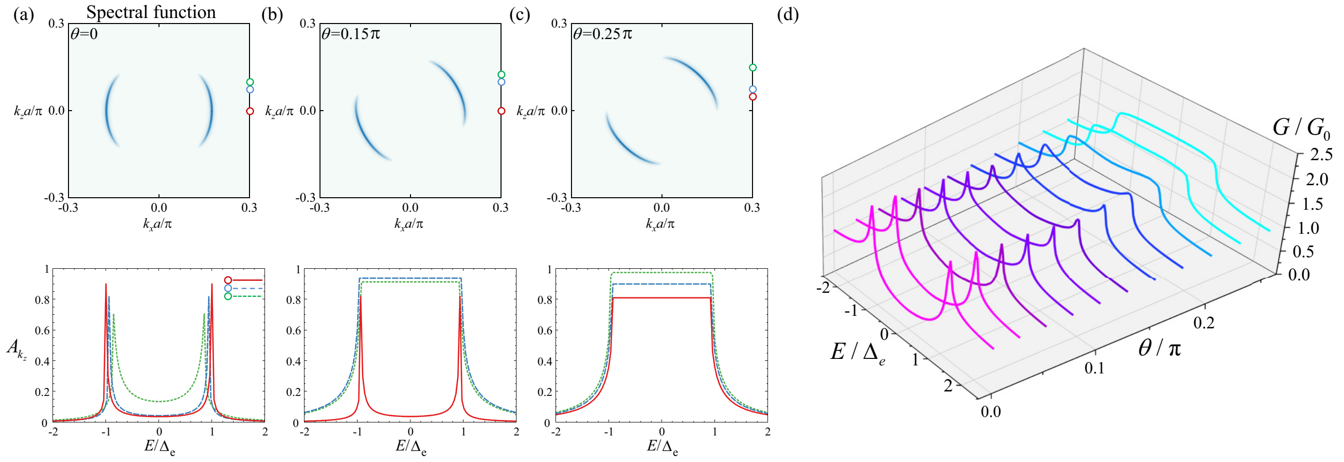

FIG. 2. (a)–(c) Upper panel: Fermi-arc spectra for different azimuthal angle θ. Lower panel: Corresponding AR probabilities for different k_z channels. (d) Crossover of the conductance spectra from suppressed to perfect AR with the variation of θ. The calculation parameters are $a = 1$ nm, $M_1 = M_2 = 1.25$ eV nm^2, $v_y = -0.66$ eV nm, $k_0 = k_1 = 0.4$ nm^{-1}, $t_N = 0.8$ eV, $t_S = 0.1$ eV, $C = 1$ eV, $\mu_1 = 2.2$ eV and $\mu_2 = 2.05$ eV, $\Delta = 5$ meV. Here, the energy unit is chosen as $\Delta_e = \Delta_e|_{k_z=0}$ for $\theta = 0$.

$\mathcal{H}_W(\boldsymbol{k})$ defines a 2D slice in momentum space. Edge states induced by the nontrivial band topology of the bulk states emerge as the k_z slice intersects the FAs under the open boundary condition [58], which provide scattering channels for electrons (holes). Throughout the work, all the results are calculated using a lattice version of this model obtained by substituting $k_{i=x,y,z} \to a^{-1}\sin k_i a$ and $k_i^2 \to 2a^{-2}(1-\cos k_i a)$, with a the lattice constant of the fictitious cubic lattice (see Appendix A for details).

We then discuss the transport process of the 2D slices with different k_z. Generally, the FA can be divided into two parts, according to whether the normal reflection channels exist or not; see Fig. 1(c). In region I, only a single chiral edge state exists for each k_z so that no normal reflection can occur; see Fig. 1(d). However, a hole channel is available for the AR, which corresponds to the electron-paired state with opposite k_z as sketched by the blue dashed circle in Fig. 1(c). As a result, perfect AR with unity probability can be realized. Such a band structure for a given k_z breaks particle-hole symmetry, which cannot be realized in any 2D system. It appears only as a subsystem of the whole 3D WSM, where two paired electrons are from opposite k_z slices carrying zero net momentum. As all the k_z channels are taken into account, the particle-hole symmetry retains. In region II, both normal reflection and AR channels exist as shown in Figs. 1(c) and 1(d), similar to a conventional metal. Given that the normal reflection generally occurs at the boundary of the S electrode due to the interface barrier or momentum mismatch, a suppression of AR is expected in region II, giving rise to two resonant peaks at the edges of the band gap.

We solve the transport problem through the surface planar junction as shown in Fig. 1(a). The N electrode deposited on top of the WSM is described by the effective Hamiltonian as $\mathcal{H}_N(\boldsymbol{k}) = (C\boldsymbol{k}^2 - \mu_N)\tau_z$ with C determined by the effective mass of the electron, μ_N is the chemical potential, and $\tau_{x,y,z}$ is the Pauli matrices in Nambu space. Similarly, the S bar is captured by $\mathcal{H}_S(\boldsymbol{k}) = (C\boldsymbol{k}^2 - \mu_S)\tau_z + \Delta\tau_x$ with a different chemical potential μ_S and a finite s-wave pair potential Δ. Due to the proximity effect, an effective superconducting gap $\Delta_e(k_z)$ can be induced in the FA under the S electrode (see Appendix B for details). We assume that the size of both strip electrodes in the z direction is much larger than the Fermi wavelength and their boundaries are smooth enough that the transverse momentum k_z is approximately conserved during scattering. Then by taking k_z as a parameter, the 3D system can be decomposed into a set of 2D slices labeled by k_z, thus simplifying the transport calculation.

III. CONDUCTANCE

We first study the transport properties of the 2D slices of the system labeled by k_z. For a hybridized square lattice, the Hamiltonian at a given k_z is set as $\mathcal{H}_W(\boldsymbol{k})$, $\mathcal{H}_N(\boldsymbol{k})$, and $\mathcal{H}_S(\boldsymbol{k})$ for different parts. The coupling between the N (S) and the WSM is described by coupling strength t_N (t_S) between two outmost lattice layers of contacting areas. The lattice Hamiltonian for calculation is elucidated in Appendix A. The thickness of the WSM and the N (S) electrode in the y direction is 100 and 50 nm, respectively. The width of the hopping area between the WSM and the N electrode is $W = 20$ nm, the separation between two electrodes is $L = 40$ nm [cf. Fig. 1(b)] and the hopping between the WSM and the S electrode extends to infinity in the x direction. An on-site potential of 6 eV is introduced at the boundary line of the S electrode to simulate the interface barrier or the momentum mismatch in the planar junction. Both the WSM and N (S) electrodes connect to the leads extending to infinity in the $\pm x$ directions. In the energy scale smaller than $\Delta_e(k_z)$, the current is dominated by the AR. For the 2D lattice with fixed k_z, the scattering process can be described by

$$\begin{bmatrix}\psi_{i,e}^{\mathrm{out}}\\ \psi_{i,h}^{\mathrm{out}}\end{bmatrix} = \sum_j \begin{bmatrix} r_{ee}^{ij} & r_{eh}^{ij}\\ r_{he}^{ij} & r_{hh}^{ij}\end{bmatrix}\begin{bmatrix}\psi_{j,e}^{\mathrm{in}}\\ \psi_{j,h}^{\mathrm{in}}\end{bmatrix}, \tag{2}$$

where $\psi_{i,e(h)}^{\mathrm{in(out)}}$ represents the income (outgoing) wave amplitudes of electrons (holes) at the N electrode, r_{he}^{ij} describes the scattering amplitude from electrons of channel j to holes of channel i at the same lead. Then the AR probability can be calculated by taking the trace of the electron-to-hole reflection matrix, $\mathrm{A}_{k_z}(E) = \mathrm{Tr}[\hat{r}_{he}^{\dagger}(E,k_z)\hat{r}_{he}(E,k_z)] = \sum_{i,j}|r_{he}^{ij}(E,k_z)|^2$, using KWANT [59], which describes the AR process that an electron is incident from the N electrode and a hole is reflected back. We plot $\mathrm{A}_{k_z}(E)$ in Figs. 2(a)–2(c) for different orientations of the FAs. In the limiting case of $\theta = 0$ in Fig. 2(a), all k_z is in region II, so that the AR is strongly suppressed, leaving only two resonant peaks at $E = \pm\Delta_e$. Note that $\Delta_e(k_z)$ slightly varies with k_z, so that the positions of resonant peaks for different k_z do not coincide. It stems from that the surface states labeled by k_z possess different spreading in the y direction, which determines the effective coupling between the surface states and the superconductor. Therefore, the proximity effect and the induced gap $\Delta_e(k_z)$ varies with k_z; see Appendix B for details. In a general case, e.g., $\theta = 0.15\pi$ in Fig. 2(b), region I and II coexist [cf. Fig. 1(c)]. As k_z lies in region I, perfect AR occurs with nearly unity probability within Δ_e; In stark contrast, for k_z in region II, the AR probability exhibits double-spike behavior, which indicates a strong normal reflection. In the opposite limit, e.g., $\theta = 0.25\pi$ in Fig. 2(c), all the electrons reside in region I, and so the AR probability exhibits a perfect AR plateau within Δ_e. The AR probability is slightly smaller than unity which stems from that in our simulation, the incident channels of the FA are not fully occupied by the electrons injected from the N electrod. Nevertheless, the perfect AR can be manifested in the subgap plateau of its probability.

The crossover from suppressed to perfect AR can be probed by the conductance spectra. Imposing a bias voltage V between the N and S electrodes drives a current J in the S; see Fig. 1(a). The differential conductance $G = \partial J/\partial V$ at zero temperature can be obtained by summing the contributions from all the k_z channels as

$$G(eV) = \sum_{k_z} g_{k_z}; \quad g_{k_z}(eV) = \frac{e^2}{h}\left(\mathrm{N}_{k_z} + \mathrm{A}_{k_z} - \mathrm{B}_{k_z}\right), \tag{3}$$

where the conductance g_{k_z} for each k_z channel is calculated by the Blonder-Tinkham-Klapwijk formula [60]. N_{k_z} is the number of incident channels below the Fermi energy in the N electrode and $\mathrm{B}_{k_z}(E) = \mathrm{Tr}[\hat{r}_{ee}^{\dagger}(E, k_z)\hat{r}_{ee}(E, k_z)] = \sum_{i,j} |r_{ee}^{ij}(E, k_z)|^2$ is the normal reflection probability.

The absolute value of conductance G relies on sample details such as the length of the strip electrodes, which is not important to our main conclusion. We plot the normalized conductance G/G_0 with $G_0 = G_{\Delta=0}$ in Fig. 2(d) for different θ. The conductance spectra are contributed by all the k_z channels, thus depending on the weight of two AR regions. In the limiting case of $\theta = 0$, all the k_z channels are in region II, giving rise to a double-peak structure in the conductance spectra, the conductance within the gap being strongly suppressed. As θ increases from zero, a portion of k_z channels transfer from region II to I so that the AR probability with either double-spike or plateau shape exists for different k_z channels [Fig. 2(b)]. Consequently, the conductance peaks are lowered accompanied by a rise of the conductance plateau within the gap. As θ exceeds the threshold $\tan^{-1}(k_0/k_1)$, all the electrons reside in region I with perfect AR. Therefore, the conductance exhibits a plateau within the gap corresponding to perfect AR in all the k_z channels. The crossover from the double-peak to plateau structure in the conductance spectra originates from the high anisotropy of FA configurations and thus provides a unique signature of the FA.

IV. MAGNETIC FIELD EFFECT

Such a crossover can be more easily observed by imposing a magnetic field B in the y direction. In this way, only a single sample with properly orientated planar junction is required. Here, we take $\theta = 0.15\pi$. The incident electrons in the right-moving channels will slide along the FA by the Lorentz force, leading to a switching between two AR regions. Specifically, for $B < 0$, a portion of electrons originally in region I are driven into region II, resulting in a transition from perfect to suppressed AR accordingly; see Fig. 3(a). Meanwhile, some of the electrons originally in region II are pushed into the chiral Landau bands of the bulk due to the surface-bulk connection at the Weyl points [50]; see Fig. 3(c). Those electrons cannot reach the S electrode so that they do not contribute to the current J flowing into the S. On the other hand, some of the reflected electrons also enter the bulk [cf. Fig. 3(a)] and they do affect the conductance spectra via the competition with the AR process. In short, the magnetic field increases the proportion of the transport electrons in region II but reduces the total number of current carriers. This is well reflected in the conductance spectra of Fig. 3(e), where with increasing B, there are a more visible double-peak structure and a decrease of the conductance amplitude. As B exceeds a critical value, all electrons reside in region II. If B increases further to the saturation value $B_c = \hbar K_z/(eL)$, all electrons will transfer into the bulk and there will be no surface electron transport. Here K_z is the span of the FA in the k_z direction [Fig. 3(a)] and L is the distance between the N and S electrodes [Fig, 1(b)]. For the parameters $K_z \simeq 0.71\ \mathrm{nm}^{-1}$ in Fig. 2(b) and $L = 40$ nm, the saturated magnetic field is evaluated to be $B_c \simeq 11.7$ Tesla (see Appendix C for details).

Similarly, for $B > 0$, electrons originally in region II are driven into region I [Fig. 3(b)], which induces a transition from the double-spike to plateau structure of the AR probability. Consequently, a plateaulike conductance spectrum gradually forms with increasing B, accompanied by a reduction of its overall magnitude due to the transfer of electrons from region I into the bulk [Fig. 3(d)]; see Fig. 3(f). The response of the AR spectra to the magnetic field stems from the unique surface-bulk connection so that it provides another unambiguous evidence of the FA.

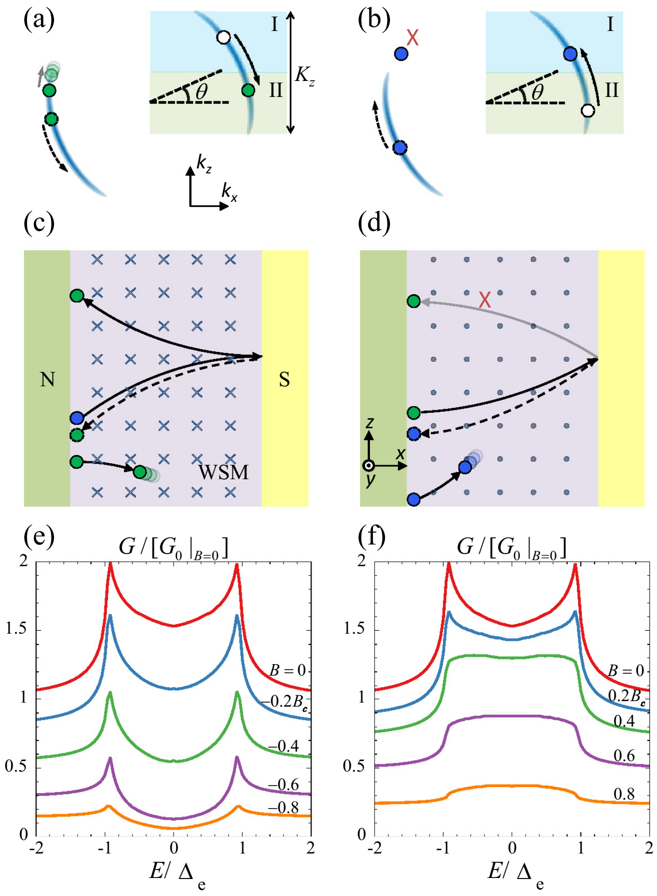

FIG. 3. (a),(b) Particles slide along the FA and switch between two AR regions driven by the Lorentz force. (c),(d) Trajectories of particles in real space corresponding to the upper panels. Conductances for different magnetic fields in the (e) $-y$ and (f) y directions. All the parameters are the same as those in Fig. 2.

In the calculation, we adopt the Landau gauge $\boldsymbol{A} = (0, 0, Bx)$ so that the Peierls substitution $\boldsymbol{k} \rightarrow -i\nabla \pm e\boldsymbol{A}/\hbar$ (taking $e > 0$) for both the electron and hole parts retains the k_z conservation. The number of electrons that do not reach the S electrode is subtracted from N_{k_z} in Eq. (3) by tracking their trajectory in the $-x$ direction on the bottom surface, and the number of electrons transferring to the bulk for the normal reflection is included in B_{k_z} by tracking their trajectory in the x direction on the bottom surface as well. To include the reduction of the conductance due to the magnetic field, all results in Figs. 3(e) and 3(f) are normalized by the same $G_0|_{B=0}$. For a strong magnetic field $B \simeq B_c$, all the incident electrons go into the bulk so that the current J flowing into the S electrode is quenched.

V. DISCUSSION

Some remarks are made below about the experimental implementation of our proposal. The surface planar NS junction can be achieved by state-of-the-art fabrication techniques [61–63]. We considered the WSM with a pair of FAs here, which have been reported in $\mathrm{NbIrTe_4}$ ($\mathrm{TaIrTe_4}$) [47,52–54], $\mathrm{WP_2}$ [64], $\mathrm{MoTe_2}$ [65], and $\mathrm{YbMnBi_2}$ [66]. The main conclusion can be generalized to the situation with more Weyl nodes straightforwardly, as the main results stem from the anisotropy of the open FAs and the proximity effect between the superconductor and the FAs, which do not rely on the number of the Weyl nodes. For the multiple pairs of Weyl nodes, the present results still hold as long as the two regions of the Andreev reflection, without or with backscattering channels [region I and II in Fig. 1(c)], can be well separated in the reciprocal space denoted by k_z, then the switching between them can be achieved in the same way by tuning θ or B. The FA with a regular shape is beneficial to our proposal, in which the monotonic change of k_z channels between two AR regions can be revealed visibly in the conductance spectra. This requires a big separation between Weyl points in momentum space [52,64,66–69]. In our calculations, for simplicity, zero chemical potential was taken in the WSM, where there is a vanishing density of bulk states. In real materials with finite density of bulk states, our main results remain unchanged as long as the FAs are well separated from the bulk states in the surface Brillouin zone. The presence of bulk states will only cause certain leakage of surface electrons, but does not change the current qualitative results. Finally, we focused on spin-degenerate FA in this work, and for the FA with fine spin textures [70,71], the analysis of AR will be modified by including the spin degree of freedom.

ACKNOWLEDGMENTS

We thank X. Wan and F. Tang for helpful discussions. This work was supported by the National Natural Science Foundation of China under Grant No. 12074172 (W.C.), the startup grant at Nanjing University (W.C.), the State Key Program for Basic Researches of China under Grants No. 2017YFA0303203 (D.Y.X.) and the Excellent Programme at Nanjing University.

APPENDIX A: LATTICE MODEL FOR NUMERICAL CALCULATION

We elucidate the model and parameters for the device sketched in Fig. 1(a). The numerical calculations are performed on a cubit lattice model of Eq. (1) through the mapping $k_{i=x,y,z} \to a^{-1}\sin k_i a$ and $k_i^2 \to 2a^{-2}(1-\cos k_i a)$, with a the lattice constant of the fictitious cubic lattice. Performing Fourier transformation in both the x and y directions yields

$$\begin{aligned} H_W^{\mathrm{latt}} &= \sum_i \psi_i^\dagger H_{ii}\psi_i + \sum_i \psi_i^\dagger H_{i,i+\hat{x}}\psi_{i+\hat{x}} \\ &\quad + \sum_i \psi_i^\dagger H_{i,i+\hat{y}}\psi_{i+\hat{y}} + \mathrm{H.c.}, \end{aligned} \tag{A1}$$

where $\psi_i = (\psi_{1,i}, \psi_{2,i})^{\mathrm{T}}$ are the Fermi operators with two pseudospin components, and the on-site and nearest-neighbor hopping matrices are

$$\begin{aligned} H_{ii} &= M_2\left(k_0^2 - \frac{4}{a^2} + \frac{2}{a^2}\cos k_z a\right)\sigma_z + M_1\left(k_1^2 - \frac{2}{a^2}\right)\sigma_x \\ H_{i,i+\hat{x}} &= \frac{M_1\sigma_x}{a^2}, \quad H_{i,i+\hat{y}} = \frac{M_2\sigma_z}{a^2} + \frac{v_y\sigma_y}{2ai}. \end{aligned} \tag{A2}$$

Note that k_z is conserved during scattering which is treated as a parameter. Similarly, the lattice models for the normal metal and superconductor are

$$\begin{aligned} H_N^{\mathrm{latt}} &= \sum_i \left(\frac{6C}{a^2} - \frac{2C}{a^2}\cos k_z a - \mu_N\right) d_i^\dagger d_i \\ &\quad - \sum_i \frac{C}{a^2}(d_i^\dagger d_{i+\hat{x}} + d_i^\dagger d_{i+\hat{y}}) + \mathrm{H.c.}, \\ H_S^{\mathrm{latt}} &= \sum_i \left(\frac{6C}{a^2} - \frac{2C}{a^2}\cos k_z a - \mu_S\right) c_i^\dagger c_i \\ &\quad - \sum_i \frac{C}{a^2}(c_i^\dagger c_{i+\hat{x}} + c_i^\dagger c_{i+\hat{y}}) + \sum_i \Delta c_i^\dagger c_i^\dagger + \mathrm{H.c.}, \end{aligned} \tag{A3}$$

where d_i, c_i are electron operators for the normal metal and the superconductor, respectively. The coupling between the outmost layers of the WSM and the N(S) is described as

$$\begin{aligned} H_T &= \sum_i t_N[d_i^\dagger \psi_{1,i+\hat{y}} + d_i^\dagger \psi_{2,i+\hat{y}}] \\ &\quad + \sum_i t_S[c_i^\dagger \psi_{1,i+\hat{y}} + c_i^\dagger \psi_{2,i+\hat{y}}] + \mathrm{H.c.}. \end{aligned} \tag{A4}$$

APPENDIX B: SUPERCONDUCTING PROXIMITY EFFECT OF THE SURFACE STATES

In this section, we employ a tunneling model description to calculate the effective pair potential $\Delta_e(k_z)$ in the surface states of the WSM induced by the superconductor deposited above. We will show that the pair potential $\Delta_e(k_z)$ generally possesses a k_z dependence. Next we work on the continuous model instead of the discrete one and the whole Hamiltonian contains three terms as

$$\begin{aligned} H &= H_S + H_W + H_t, \\ H_S &= \sum_{\boldsymbol{k}} \varepsilon_{\boldsymbol{k}} c_{\boldsymbol{k}}^\dagger c_{\boldsymbol{k}} + (\Delta c_{\boldsymbol{k}}^\dagger c_{-\boldsymbol{k}}^\dagger + \mathrm{H.c.}), \\ H_W &= \int_{-\infty}^{0} dy \sum_{\boldsymbol{k}_\parallel} \psi_{\boldsymbol{k}_\parallel}^\dagger(y) H_W^0(\boldsymbol{k}_\parallel, -i\partial_y)\psi_{\boldsymbol{k}_\parallel}(y), \\ H_t &= \sum_{\boldsymbol{k}_\parallel, k_y}\sum_{a=1,2}\int_{-\infty}^{0} dy[t(y) c_{\boldsymbol{k}}^\dagger \psi_{a\boldsymbol{k}_\parallel}(y) + \mathrm{H.c.}], \end{aligned} \tag{B1}$$

where H_S, $H_W^0(\boldsymbol{k}_\parallel, -i\partial_y)$ [cf. Eq. (1)] and H_t describe the superconductor, the WSM, and the coupling between them with the strength $t(y)$, respectively, and $\psi_{\boldsymbol{k}_\parallel}(y) = [\psi_{1\boldsymbol{k}_\parallel}(y), \psi_{2\boldsymbol{k}_\parallel}(y)]^{\mathrm{T}}$ is the two-component Fermi operator in the WSM that is interpreted by the in-plane momentum $\boldsymbol{k}_\parallel = (k_x, k_z)$ and spatial coordinate y in the perpendicular direction. We assume a good quality of contact between the

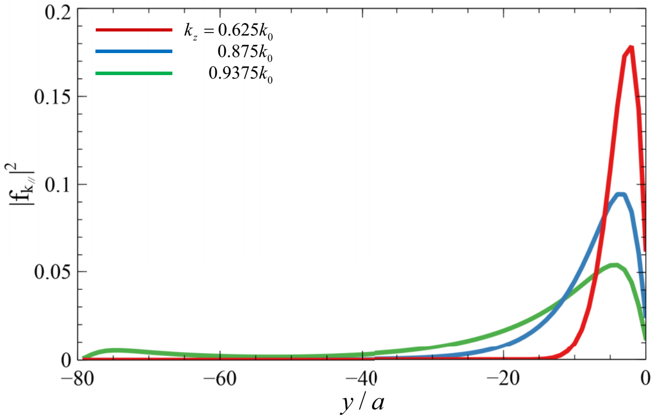

FIG. 4. The dispersion of $f_{\boldsymbol{k}_\parallel}$ along the y direction for different k_z channels, here $k_x = k_1$, other parameters are the same as those in Fig. 2.

superconductor and the WSM such that $\boldsymbol{k}_\parallel = (k_x, k_z)$ is conserved during tunneling.

The coupling between the superconductor and the surface states strongly relies on the spatial distribution of the latter, which gives rise to the proximity effect. Moreover, the pairing occurs mainly around the Fermi level (here it is the zero energy) so that it is sufficient to look at the surface states at the Fermi energy. We solve the surface states for a semi-infinite Weyl semimetal with the upper surface set to $y = 0$. Applying the substitution $k_y \to -i\partial_y$ to Eq. (1) and taking $v_y = 1$ for simplicity, the surface states $\phi_{\boldsymbol{k}_\parallel}(y)$ with zero energy and $k_z \in (-k_0, k_0)$ is solved by the equation $H(k_x, -i\partial_y, k_z)\phi_{\boldsymbol{k}_\parallel}(y) = 0$, which gives

$$\phi_{\boldsymbol{k}_\parallel}(y) = f_{k_z}(y)\begin{pmatrix}\alpha\\ \beta\end{pmatrix}, \tag{B2}$$

with $f_{k_z}(y) = e^{\lambda_1 y} - e^{\lambda_2 y}$ the distribution function in the y direction and $\lambda_{1,2} = \frac{1}{2|M_2|} \pm \sqrt{\frac{1}{4M_2^2} + k_z^2 - k_0^2}$. The spinor $(\alpha, \beta)^{\mathrm{T}}$ is a function of $\boldsymbol{k}_\parallel$, with $k_x = \pm k_1$ corresponding to two straight Fermi arcs solved by the continuous model (1). One can see that $f_{k_z}(y)$ exhibits a k_z dependence, which is also shown in the Fig. 4. Physically, the 2D slices labeled by k_z have different mass terms or gaps in the bulk, which lead to different spreading of the surface states. Here only the low energy surface states are of interest and then H_W^0 reduces to

$$H_{\text{surf}} = \sum_{\boldsymbol{k}_\parallel} \epsilon_{\boldsymbol{k}_\parallel} \gamma_{\boldsymbol{k}_\parallel}^\dagger \gamma_{\boldsymbol{k}_\parallel},$$
$$\gamma_{\boldsymbol{k}_\parallel}^\dagger = \int dy f_{k_z}(y)[\alpha\psi_{1\boldsymbol{k}_\parallel}^\dagger(y) + \beta\psi_{2\boldsymbol{k}_\parallel}^\dagger(y)], \tag{B3}$$

with $\epsilon_{\boldsymbol{k}_\parallel}$ the energy of the surface states for $k_z \in (-k_0, k_0)$, and $\gamma_{\boldsymbol{k}_\parallel}$ the corresponding Fermi operator.

For the low-energy scale of order Δ, we can interpret the field operator $\psi_{\boldsymbol{k}_\parallel}(y)$ by the surface states as

$$\psi_{\boldsymbol{k}_\parallel}(y) \simeq \gamma_{\boldsymbol{k}_\parallel}\phi_{\boldsymbol{k}_\parallel}(y). \tag{B4}$$

Then the tunneling term reduces to

$$H_t = \sum_{\boldsymbol{k}_\parallel, k_y} V_{\boldsymbol{k}_\parallel} c_{\boldsymbol{k}}^\dagger \gamma_{\boldsymbol{k}_\parallel} + \text{H.c.},$$
$$V_{\boldsymbol{k}_\parallel} = \int dy t(y) f_{k_z}(y)(\alpha + \beta), \tag{B5}$$

where $V_{\boldsymbol{k}_\parallel}$ is the effective coupling between the surface states and the superconductor. It strongly depends on the distribution function $f_{k_z}(y)$ of the surface states and thus on k_z. Starting from the effective tunneling Hamiltonian, one can solve the self-energy of the surface states due to its proximity to the superconductor.

The self-energy of the surface states in Nambu space can be expressed as

$$\Sigma_{\text{surf}}(\omega) = \hat{T}^\dagger g_S(\omega)\hat{T},\ g_S(\boldsymbol{k};\omega) = \frac{\omega + \varepsilon_{\boldsymbol{k}}\tau_z + \Delta\tau_x}{\omega^2 - \varepsilon_{\boldsymbol{k}}^2 - \Delta^2}, \tag{B6}$$

where $g_S(\boldsymbol{k}, \omega)$ is the bare Green's function in the superconductor and $\hat{T} = V_{\boldsymbol{k}_\parallel}\tau_z$ represents the tunneling terms from the surface states to the superconductor in H_t. We obtain the self-energy after some algebra as

$$\Sigma_{\text{surf}}(\boldsymbol{k}_\parallel, \omega) = |V_{\boldsymbol{k}_\parallel}|^2 \sum_{k_y} \tau_z g_S(\boldsymbol{k}, \omega)\tau_z. \tag{B7}$$

We define the 1D density of states as $N_{\boldsymbol{k}_\parallel}(\varepsilon) = [\partial\varepsilon/\partial k_y]^{-1}$ and take its value approximately to be that at the Fermi energy $N_{\boldsymbol{k}_\parallel}(0)$, which yields

$$\Sigma_{\text{surf}}(\boldsymbol{k}_\parallel, \omega) = -\xi(\omega)[\omega - \Delta\tau_x],$$
$$\xi(\omega) = |V_{\boldsymbol{k}_\parallel}|^2\pi N_{\boldsymbol{k}_\parallel}(0)(\Delta^2 - \omega^2)^{-\frac{1}{2}}. \tag{B8}$$

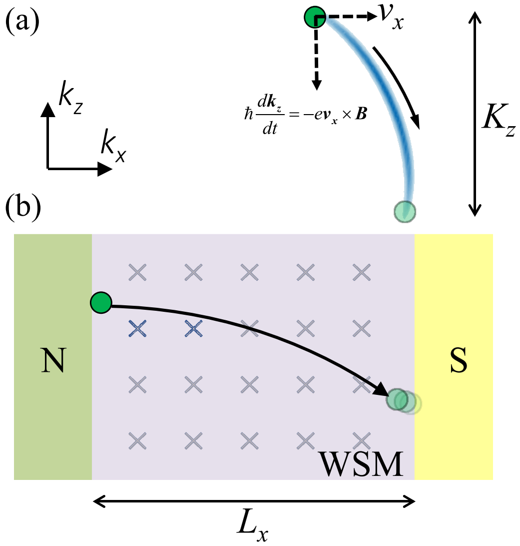

FIG. 5. (a) Particles slide along the FA and pushed into the Weyl node by the Lorentz force. (b) The electron trail in real space of the critical case that the incident electrons with k_z at a Weyl node are pushed into the other Weyl node just before coming out of the magnetic field, corresponding to (a).

Then we obtain the full Green's function of the surface states as

$$\begin{aligned} G_{\rm surf}(\boldsymbol{k}_\parallel,\omega) &= \frac{\chi(\omega)}{\omega - H^{\rm eff}_{\rm surf}},\\ H^{\rm eff}_{\rm surf} &= \epsilon_{\boldsymbol{k}_\parallel}\chi(\omega)\tau_z + \Delta_e\tau_x,\\ \chi(\omega) &= 1/(1+\xi), \end{aligned} \tag{B9}$$

where the effective Hamiltonian of the surface states $H^{\rm eff}_{\rm surf}$ involves the proximity effect, from which we obtain the pairing potential in the surface states as

$$\Delta_e(k_z,\omega) = \frac{\xi}{1+\xi}\Delta. \tag{B10}$$

We focus on the weak coupling limit $\xi << 1$ and the effective pairing potential reduces to

$$\Delta_e(k_z,\omega) \simeq \xi(k_z,\omega)\Delta. \tag{B11}$$

Note from Eq. (B8) that $\xi \propto |V_{\boldsymbol{k}_\parallel}|^2$ which increases as k_z deviates from $\pm k_0$, so that $\Delta_e(k_z)$ also varies with k_z, which explains the slight splitting of the resonant peaks for different k_z slice in Fig. 2(a).

APPENDIX C: SEMICLASSICAL DESCRIPTION OF THE MAGNETIC FIELD EFFECTS

In this section, we evaluate the saturated magnetic field B_c based on a semiclassical picture. As shown in Fig. 5(a), once the magnetic field is employed, the incident electrons in the right-moving channels will be driven by the Lorentz force and slide along the Fermi arc. B_c is the critical value such that all electrons incident from the normal metal arrive at the Weyl node and transfer into the bulk Landau band before they reach the superconductor. The semiclassical equation of motion is given by

$$\hbar\dot{\boldsymbol{k}}_z = (-e)\boldsymbol{v_x}\times\boldsymbol{B}, \tag{C1}$$

where v_x is the x-direction velocity. Integrating the equation on both sides yields $\hbar\Delta k_z = -e\Delta x B$, which relates to the change of the momentum k_z in the z direction and the displacement Δx in the x direction. The saturated magnetic field is thus given by

$$B_c = \frac{\hbar K_z}{eL_x}. \tag{C2}$$

---

[1] H. Weyl, Proc. Nat. Acad. Sci. USA **15**, 323 (1929).

[2] N. P. Armitage, E. J. Mele, and A. Vishwanath, Rev. Mod. Phys. **90**, 015001 (2018).

[3] T. Kajita, Rev. Mod. Phys. **88**, 030501 (2016).

[4] A. B. McDonald, Rev. Mod. Phys. **88**, 030502 (2016).

[5] X. Wan, A. M. Turner, A. Vishwanath, and S. Y. Savrasov, Phys. Rev. B **83**, 205101 (2011).

[6] S. Murakami, New J. Phys. **9**, 356 (2007).

[7] A. A. Burkov and L. Balents, Phys. Rev. Lett. **107**, 127205 (2011).

[8] H. Weng, C. Fang, Z. Fang, B. A. Bernevig, and X. Dai, Phys. Rev. X **5**, 011029 (2015).

[9] S.-M. Huang, S.-Y. Xu, I. Belopolski, C.-C. Lee, G. Chang, B. Wang, N. Alidoust, G. Bian, M. Neupane, C. Zhang *et al.*, Nat. Commun. **6**, 7373 (2015).

[10] B. Q. Lv, H. M. Weng, B. B. Fu, X. P. Wang, H. Miao, J. Ma, P. Richard, X. C. Huang, L. X. Zhao, G. F. Chen, Z. Fang, X. Dai, T. Qian, and H. Ding, Phys. Rev. X **5**, 031013 (2015).

[11] S.-Y. Xu, I. Belopolski, N. Alidoust, M. Neupane, G. Bian, C. Zhang, R. Sankar, G. Chang, Z. Yuan, C.-C. Lee *et al.*, Science **349**, 613 (2015).

[12] S.-Y. Xu, N. Alidoust, I. Belopolski, Z. Yuan, G. Bian, T.-R. Chang, H. Zheng, V. N. Strocov, D. S. Sanchez, G. Chang *et al.*, Nat. Phys. **11**, 748 (2015).

[13] S.-Y. Xu, I. Belopolski, D. S. Sanchez, C. Zhang, G. Chang, C. Guo, G. Bian, Z. Yuan, H. Lu, T.-R. Chang *et al.*, Sci. Adv. **1**, e1501092 (2015).

[14] N. Xu, H. Weng, B. Lv, C. E. Matt, J. Park, F. Bisti, V. N. Strocov, D. Gawryluk, E. Pomjakushina, K. Conder *et al.*, Nat. Commun. **7**, 11006 (2016).

[15] K. Deng, G. Wan, P. Deng, K. Zhang, S. Ding, E. Wang, M. Yan, H. Huang, H. Zhang, Z. Xu *et al.*, Nat. Phys. **12**, 1105 (2016).

[16] L. Yang, Z. Liu, Y. Sun, H. Peng, H. Yang, T. Zhang, B. Zhou, Y. Zhang, Y. Guo, M. Rahn *et al.*, Nat. Phys. **11**, 728 (2015).

[17] L. Huang, T. M. McCormick, M. Ochi, Z. Zhao, M.-T. Suzuki, R. Arita, Y. Wu, D. Mou, H. Cao, J. Yan *et al.*, Nat. Mater. **15**, 1155 (2016).

[18] A. Tamai, Q. S. Wu, I. Cucchi, F. Y. Bruno, S. Riccò, T. K. Kim, M. Hoesch, C. Barreteau, E. Giannini, C. Besnard, A. A. Soluyanov, and F. Baumberger, Phys. Rev. X **6**, 031021 (2016).

[19] J. Jiang, Z. Liu, Y. Sun, H. Yang, C. Rajamathi, Y. Qi, L. Yang, C. Chen, H. Peng, C. Hwang *et al.*, Nat. Commun. **8**, 13973 (2017).

[20] I. Belopolski, D. S. Sanchez, Y. Ishida, X. Pan, P. Yu, S.-Y. Xu, G. Chang, T.-R. Chang, H. Zheng, N. Alidoust *et al.*, Nat. Commun. **7**, 13643 (2016).

[21] B. Lv, N. Xu, H. Weng, J. Ma, P. Richard, X. Huang, L. Zhao, G. Chen, C. Matt, F. Bisti *et al.*, Nat. Phys. **11**, 724 (2015).

[22] Junwei, C. Liu, L. Fang, and Fu, Chin. Phys. B **28**, 047301 (2019).

[23] S. L. Adler, Phys. Rev. **177**, 2426 (1969).

[24] J. S. Bell and R. Jackiw, Il Nuovo Cimento A (1965-1970) **60**, 47 (1969).

[25] H. B. Nielsen and M. Ninomiya, Phys. Lett. B **130**, 389 (1983).

[26] A. A. Zyuzin and A. A. Burkov, Phys. Rev. B **86**, 115133 (2012).

[27] V. Aji, Phys. Rev. B **85**, 241101(R) (2012).

[28] D. T. Son and B. Z. Spivak, Phys. Rev. B **88**, 104412 (2013).

[29] M. N. Chernodub, A. Cortijo, A. G. Grushin, K. Landsteiner, and M. A. H. Vozmediano, Phys. Rev. B **89**, 081407(R) (2014).

[30] J.-H. Zhou, H. Jiang, Q. Niu, and J.-R. Shi, Chin. Phys. Lett. **30**, 027101 (2013).
[31] A. Burkov, J. Phys.: Condens. Matter **27**, 113201 (2015).
[32] J. Ma and D. A. Pesin, Phys. Rev. B **92**, 235205 (2015).
[33] S. Zhong, J. E. Moore, and I. Souza, Phys. Rev. Lett. **116**, 077201 (2016).
[34] B. Z. Spivak and A. V. Andreev, Phys. Rev. B **93**, 085107 (2016).
[35] M. Hirschberger, S. Kushwaha, Z. Wang, Q. Gibson, S. Liang, C. A. Belvin, B. A. Bernevig, R. J. Cava, and N. P. Ong, Nat. Mater. **15**, 1161 (2016).
[36] X. Huang, L. Zhao, Y. Long, P. Wang, D. Chen, Z. Yang, H. Liang, M. Xue, H. Weng, Z. Fang, X. Dai, and G. Chen, Phys. Rev. X **5**, 031023 (2015).
[37] C. Shekhar, A. K. Nayak, Y. Sun, M. Schmidt, M. Nicklas, I. Leermakers, U. Zeitler, Y. Skourski, J. Wosnitza, Z. Liu *et al.*, Nat. Phys. **11**, 645 (2015).
[38] J. Du, H. Wang, Q. Chen, Q. Mao, R. Khan, B. Xu, Y. Zhou, Y. Zhang, J. Yang, B. Chen *et al.*, Sci. China Phys. Mech. Astron. **59**, 657406 (2016).
[39] Z. Wang, Y. Zheng, Z. Shen, Y. Lu, H. Fang, F. Sheng, Y. Zhou, X. Yang, Y. Li, C. Feng, and Z.-A. Xu, Phys. Rev. B **93**, 121112(R) (2016).
[40] C.-L. Zhang, S.-Y. Xu, I. Belopolski, Z. Yuan, Z. Lin, B. Tong, G. Bian, N. Alidoust, C.-C. Lee, S.-M. Huang *et al.*, Nat. Commun. **7**, 10735 (2016).
[41] A. Chen and M. Franz, Phys. Rev. B **93**, 201105(R) (2016).
[42] S. Uchida, T. Habe, and Y. Asano, J. Phys. Soc. Jpn. **83**, 064711 (2014).
[43] S.-B. Zhang, F. Dolcini, D. Breunig, and B. Trauzettel, Phys. Rev. B **97**, 041116(R) (2018).
[44] D. Breunig, S.-B. Zhang, M. Stehno, and B. Trauzettel, Phys. Rev. B **99**, 174501 (2019).
[45] N. Morali, R. Batabyal, P. K. Nag, E. Liu, Q. Xu, Y. Sun, B. Yan, C. Felser, N. Avraham, and H. Beidenkopf, Science **365**, 1286 (2019).
[46] H. Yang, L. Yang, Z. Liu, Y. Sun, C. Chen, H. Peng, M. Schmidt, D. Prabhakaran, B. Bernevig, C. Felser *et al.*, Nat. Commun. **10**, 1 (2019).
[47] S. A. Ekahana, Y. W. Li, Y. Sun, H. Namiki, H. F. Yang, J. Jiang, L. X. Yang, W. J. Shi, C. F. Zhang, D. Pei, C. Chen, T. Sasagawa, C. Felser, B. H. Yan, Z. K. Liu, and Y. L. Chen, Phys. Rev. B **102**, 085126 (2020).
[48] W. Chen, K. Luo, L. Li, and O. Zilberberg, Phys. Rev. Lett. **121**, 166802 (2018).
[49] G. Chen, O. Zilberberg, and W. Chen, Phys. Rev. B **101**, 125407 (2020).
[50] A. C. Potter, I. Kimchi, and A. Vishwanath, Nat. Commun. **5**, 1 (2014).
[51] W. Chen, L. Jiang, R. Shen, L. Sheng, B. Wang, and D. Xing, EPL (Europhysics Letters) **103**, 27006 (2013).
[52] K. Koepernik, D. Kasinathan, D. V. Efremov, S. Khim, S. Borisenko, B. Büchner, and J. van den Brink, Phys. Rev. B **93**, 201101(R) (2016).
[53] I. Belopolski, P. Yu, D. S. Sanchez, Y. Ishida, T.-R. Chang, S. S. Zhang, S.-Y. Xu, H. Zheng, G. Chang, G. Bian *et al.*, Nat. Commun. **8**, 1 (2017).
[54] E. Haubold, K. Koepernik, D. Efremov, S. Khim, A. Fedorov, Y. Kushnirenko, J. van den Brink, S. Wurmehl, B. Büchner, T. K. Kim, M. Hoesch, K. Sumida, K. Taguchi, T. Yoshikawa, A. Kimura, T. Okuda, and S. V. Borisenko, Phys. Rev. B **95**, 241108(R) (2017).
[55] M. Bianchi, D. Guan, S. Bao, J. Mi, B. B. Iversen, P. D. King, and P. Hofmann, Nat. Commun. **1**, 1 (2010).
[56] P. D. C. King, R. C. Hatch, M. Bianchi, R. Ovsyannikov, C. Lupulescu, G. Landolt, B. Slomski, J. H. Dil, D. Guan, J. L. Mi, E. D. L. Rienks, J. Fink, A. Lindblad, S. Svensson, S. Bao, G. Balakrishnan, B. B. Iversen, J. Osterwalder, W. Eberhardt, F. Baumberger, and P. Hofmann, Phys. Rev. Lett. **107**, 096802 (2011).
[57] H. M. Benia, C. Lin, K. Kern, and C. R. Ast, Phys. Rev. Lett. **107**, 177602 (2011).
[58] K.-Y. Yang, Y.-M. Lu, and Y. Ran, Phys. Rev. B **84**, 075129 (2011).
[59] C. W. Groth, M. Wimmer, A. R. Akhmerov, and X. Waintal, New J. Phys. **16**, 063065 (2014).
[60] G. E. Blonder, M. Tinkham, and T. M. Klapwijk, Phys. Rev. B **25**, 4515 (1982).
[61] C.-Z. Li, A.-Q. Wang, C. Li, W.-Z. Zheng, A. Brinkman, D.-P. Yu, and Z.-M. Liao, Nat. Commun. **11**, 1150 (2020).
[62] A. Q. Chen, M. J. Park, S. T. Gill, Y. Xiao, D. Reig-i Plessis, G. J. MacDougall, M. J. Gilbert, and N. Mason, Nat. Commun. **9**, 1 (2018).
[63] S. Ghatak, O. Breunig, F. Yang, Z. Wang, A. A. Taskin, and Y. Ando, Nano Lett. **18**, 5124 (2018).
[64] M.-Y. Yao, N. Xu, Q. S. Wu, G. Autès, N. Kumar, V. N. Strocov, N. C. Plumb, M. Radovic, O. V. Yazyev, C. Felser, J. Mesot, and M. Shi, Phys. Rev. Lett. **122**, 176402 (2019).
[65] Z. Wang, D. Gresch, A. A. Soluyanov, W. Xie, S. Kushwaha, X. Dai, M. Troyer, R. J. Cava, and B. A. Bernevig, Phys. Rev. Lett. **117**, 056805 (2016).
[66] S. Borisenko, D. Evtushinsky, Q. Gibson, A. Yaresko, K. Koepernik, T. Kim, M. Ali, J. van den Brink, M. Hoesch, A. Fedorov *et al.*, Nat. Commun. **10**, 1 (2019).
[67] Y. Sun, S.-C. Wu, M. N. Ali, C. Felser, and B. Yan, Phys. Rev. B **92**, 161107(R) (2015).
[68] G. Chang, S.-Y. Xu, D. S. Sanchez, S.-M. Huang, C.-C. Lee, T.-R. Chang, G. Bian, H. Zheng, I. Belopolski, N. Alidoust, H.-T. Jeng, A. Bansil, H. Lin, and M. Z. Hasan, Sci. Adv. **2**, e1600295 (2016).
[69] E. J. Sie, C. M. Nyby, C. Pemmaraju, S. J. Park, X. Shen, J. Yang, M. C. Hoffmann, B. Ofori-Okai, R. Li, A. H. Reid *et al.*, Nature (London) **565**, 61 (2019).
[70] B. Q. Lv, S. Muff, T. Qian, Z. D. Song, S. M. Nie, N. Xu, P. Richard, C. E. Matt, N. C. Plumb, L. X. Zhao, G. F. Chen, Z. Fang, X. Dai, J. H. Dil, J. Mesot, M. Shi, H. M. Weng, and H. Ding, Phys. Rev. Lett. **115**, 217601 (2015).
[71] S.-Y. Xu, I. Belopolski, D. S. Sanchez, M. Neupane, G. Chang, K. Yaji, Z. Yuan, C. Zhang, K. Kuroda, G. Bian, C. Guo, H. Lu, T.-R. Chang, N. Alidoust, H. Zheng, C.-C. Lee, S.-M. Huang, C.-H. Hsu, H.-T. Jeng, A. Bansil, T. Neupert, F. Komori, T. Kondo, S. Shin, H. Lin, S. Jia, and M. Z. Hasan, Phys. Rev. Lett. **116**, 096801 (2016).